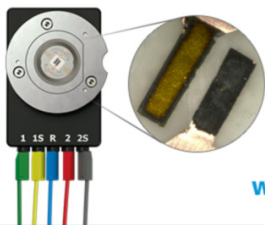# Understanding the Correlation between Lithium Dendrite Growth and Local Material Properties by Machine Learning

View the article online for updates and enhancements.

CrossMark

Understanding the Correlation between Lithium Dendrite Growth and Local Material Properties by Machine Learning

Yirui Ma,[1] **Tianwei Jin,**[1] **Rishav Choudhury,**[1] **Qian Cheng,**[1] **Yupeng Miao,**[2]
Changxi Zheng,[3] **Wei Min,**[2] **and Yuan Yang**[1,z]

[1]*Program of Materials Science and Engineering, Department of Applied Physics and Applied Mathematics, Columbia University, New York, NY 10027, United States of America*
[2]*Department of Chemistry, Columbia University, New York, NY 10027, United States of America*
[3]*Department of Computer Science, Columbia University, New York, NY 10027, United States of America*

Lithium metal batteries are attractive for next-generation energy storage because of their high energy density. A major obstacle to their commercialization is the uncontrollable growth of lithium dendrites, which arises from complicated but poorly understood interactions at the electrolyte/electrode interface. In this work, we use a machine learning-based artificial neural network (ANN) model to explore how the lithium growth rate is affected by local material properties, such as surface curvature, ion concentration in the electrolyte, and the lithium growth rates at previous moments. The ion concentration in the electrolyte was acquired by Stimulated Raman Scattering Microscopy, which is often missing in past experimental data-based modeling. The ANN network reached a high correlation coefficient of 0.8 between predicted and experimental values. Further sensitivity analysis based on the ANN model demonstrated that the salt concentration and concentration gradient, as well as the prior lithium growth rate, have the highest impacts on the lithium dendrite growth rate at the next moment. This work shows the potential capability of the ANN model to forecast lithium growth rate, and unveil the inner dependency of the lithium dendrite growth rate on various factors.
© 2021 The Electrochemical Society ("ECS"). Published on behalf of ECS by IOP Publishing Limited. [DOI: 10.1149/1945-7111/ac201d]

Lithium metal batteries are attractive for energy storage due to their high gravimetric and volumetric energy densities.[1–4] However, one of the major obstacles to deploying lithium metal batteries is the uncontrollable growth of lithium dendrites.[5–8] In the past several decades, various models have been developed to understand underlying mechanisms of lithium dendrite growth, and these models took SEI compositions,[9,10] ion transport in electrolytes,[11–14] mechanics,[15] electronic conductivity,[16,17] and space charge[18,19] into account. For example, Wu, B., et al. showed that high SEI impedance increase es the difficulty of lithium dendrite growth in one direction, causing branch-like structures to form instead.[10] Jana, A., et al. illustrated that an uneven electrical field causes rapid growth of dendrite tips.[19] However, these models typically simulated simplified geometries, instead of analyzing real experimental data. This is partially due to the difficulty in observing dendrite growth and other key properties influencing this process, such as SEI compositions and dynamic ion concentrations in the electrolyte.[20–22]

Recently, the authors used Stimulated Raman Scattering (SRS) microscopy (Fig. 1a) to image lithium dendrite growth and ion concentration in an electrolyte simultaneously.[23,24] In an SRS microscope, the synergy of two synchronized laser beams amplifies Raman signals by up to 10^8 times, leading to ultrafast imaging speed ($\sim 10^3$ faster than conventional spontaneous Raman imaging).[25,26] Therefore, we are able to observe dynamic dendrite growth and ion depletion together. Previous linear regression-based analysis showed that upon ion depletion, the correlation coefficient between the local lithium dendrite growth rate (v) and the local Li^+ ion concentration $10\,\mu m$ away from the Li/electrolyte interface ($[Li^+]_{10\mu m}$) becomes higher, increasing from 0.29 at no ion depletion to 0.84 at full ion depletion.[27]

However, such a simple regression analysis is rudimental, and it is obvious that the relation between v and ion depletion is nonlinear. Moreover, SEI heterogeneity is hidden information that does not show up in SRS images. The artificial neural network (ANN) model may be helpful to study such complex relations,[28] since it is powerful enough to capture hidden connections between different parameters, and directly establish the relation between causes and effects in relatively sophisticated systems, especially when a large quantity of data is available. ANN has already been used in a wide range of engineering topics, such as estimation of rock parameters, prediction of wastewater treatment plant performance, and compound equilibrium prediction.[29–32] In the field of energy storage, ANN has also been explored for battery life prediction and state of charge estimation.[33–36]

In this study, as SRS images provide a reasonable amount of data for machine learning, we developed a two-layer ANN model to better understand the growth mechanism of lithium dendrites in Li/ gel electrolyte/Li symmetric cells. As shown in Fig. 1c, we processed SRS raw images to reduce noise and identified the Li/ electrolyte interface first, followed by extracting seven key physical features at different moments. Next, a feed-forward ANN model using a backpropagation algorithm was established and optimized, which showed a reasonable accuracy to predict lithium dendrite growth rate (v) at the next moment. Moreover, we further probed the structure of ANN and performed a sensitivity analysis to understand the significance and relevance of selected features to v at the next moment. The results of sensitivity analysis confirm the previous study that Li^+ concentration ($[Li^+]$) at the vicinity of the Li/ electrolyte interface is strongly connected to v at the next moment.[27] Moreover, v is also affected by lithium growth rates at prior moments. Our ANN model acts as a first step to understand lithium dendrite growth by machine learning algorithms. With more subtle and advanced ANN structures and more informative experimental data, machine learning techniques could help better understand this long-lasting challenge in energy storage.

Methods

SRS image acquisition.—The same protocols and setups were used as our previous report.[27] Briefly, a Li/gel electrolyte/Li symmetric cell sealed between two pieces of glass slides was placed under an SRS microscope. The gel electrolyte is 0.33 M LiBOB in tetraethylene glycol dimethyl ether (TEGDME) with 22 wt% poly (vinylidene fluoride-cohexa-fluoropropylene) (PVdF-HFP). The SRS microscope monitored the Raman peak of Li bis(oxalato)borate (LiBOB) at $1830\ cm^{-1}$ to obtain the concentration of BOB^-, which is equivalent to the concentration of Li^+ due to the requirement of charge neutrality.[37,38] Meanwhile, SRS images can also capture the interface between solid lithium dendrites and the gel electrolyte simultaneously.[27] Due to the fast scanning rate of SRS microscopy,

[z]E-mail: yy2664@columbia.edu
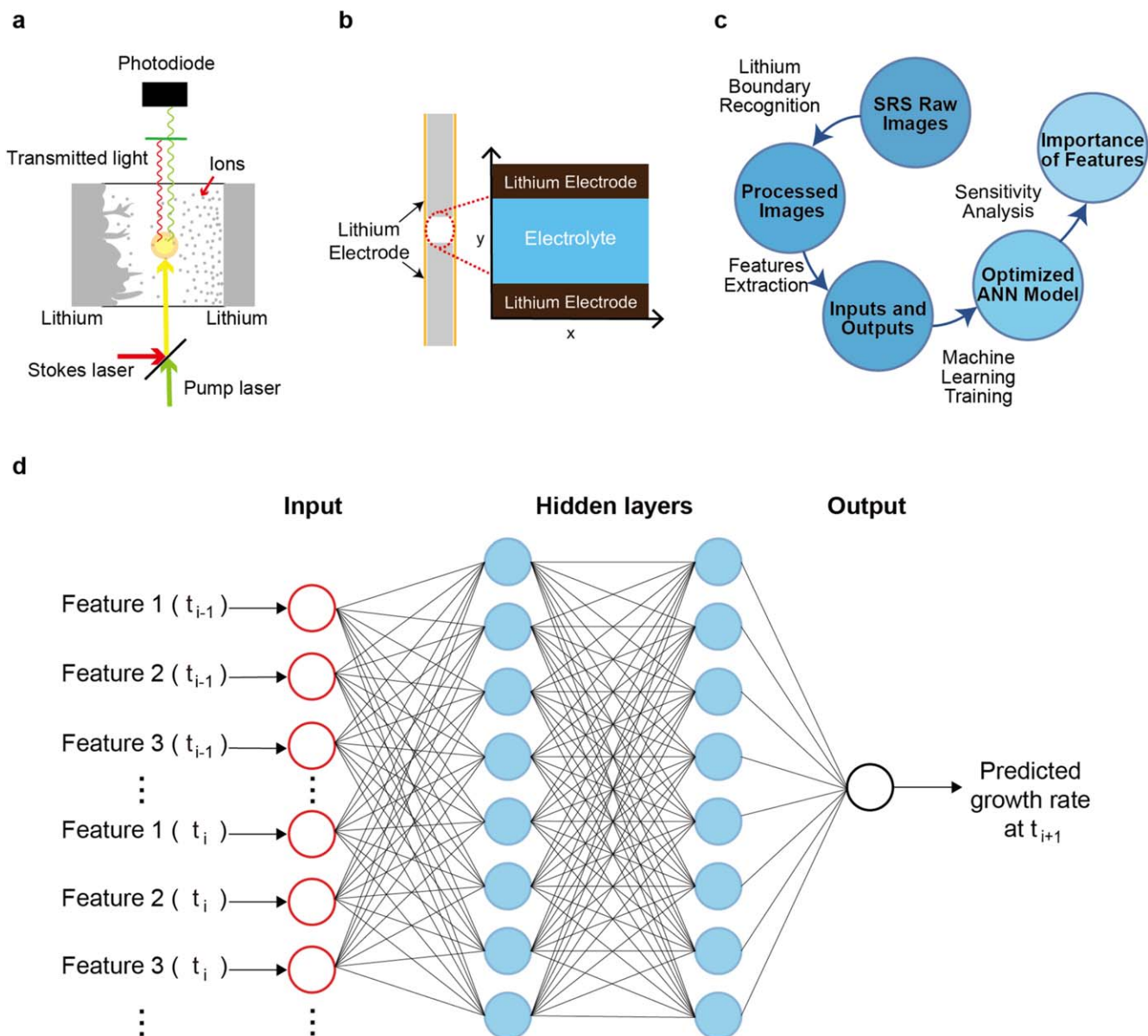
Figure 1. (a) A schematic illustration of the SRS imaging setup. The two lasers are Stokes laser and pump laser. Detailed information can be found in the supporting information. (b) A schematic illustration of a Li/Li symmetric cell and the corresponding coordination setting. The Li/electrolyte interface is along the x direction while the lithium dendrite grows along the y direction. (c) An ANN model that predicts v and performs consequent sensitivity analysis. The raw images were first captured by an SRS microscope. Then the lithium metal/electrolyte interface was identified, followed by extracting key features, and establishing an ANN to correlate v and key features. In the end, the optimized ANN model was used for sensitivity analysis, which helps understand the dependency of v on each feature. (d) The network structure of a feedforward ANN with two hidden layers and eight neurons in each layer ([8, 8]). The inputs are the seven features at the prior two timesteps t_{i-1} and t_i and the output is the predicted lithium growth rate v at the next timestep t_{i+1}.

each 256×256 2D image takes only $0.1 \sim 1$ s to capture. After the acquisition, the SRS intensities were converted into 8-bit grayscale (0–255) for image processing in the following steps.

As the spatial resolution of our SRS microscope is $\sim$500 nm, and v is in the order of $\sim$1 μm min^{-1}, an interval of five minutes was used to ensure the accuracy of v. Three sets of data from different experiments were used in the modeling, where each set includes data from the beginning (current was applied) to the end (cell voltage increased sharply). A representative voltage profile is shown in Fig. S1 (available online at stacks.iop.org/JES/168/090523/mmedia). Data set 1 is composed of sixteen images with an initial current density of 0.6 mA cm^{-2}, while data set 2 and 3 contain five images for each with a current density of 1.3 mA cm^{-2}. In each data set, the time of the n images are denoted as $t_1, t_2, \ldots t_n$, respectively. The

difference in data size originates from the different total durations of lithium deposition. As we used data at two prior moments (t_i and t_{i-1}) to predict v at the next moment t_{i+1}, there are a total of $(14 + 3 + 3) \times 200 = 4,000$ data points for the machine learning model.

Image processing and parameter extraction.—The first step in image processing was to determine the interface between lithium metal and the electrolyte. Due to strong non-linear light scattering at the lithium metal surface, the SRS signal is saturated at this interface, which appears as $\sim$255 in the gray-scale images. Therefore, a threshold of 230 was used to identify this interface. The identified lithium metal/electrolyte interface in an SRS image is denoted as $y = y(x, t)$, where y is the direction perpendicular to the lithium surface, as defined in Fig. 1b. Then the gray values in the

Table I. The brief description and mathematical expression of seven key features.

Feature	Description	Mathematical expression	Explanation
1	Up curvature	$\left(\dfrac{\partial y}{\partial x}\right)_{x=x_0-1}$	The curvature at $x = x_0 - 1$
2	Down curvature	$\left(\dfrac{\partial y}{\partial x}\right)_{x=x_0+1}$	The curvature at $x = x_0 + 1$
3	Curvature	$\left(\dfrac{\partial y}{\partial x}\right)_{x=x_0}$	The curvature at $x = x_0$
4	[Li$^+$] at the interface	$c(x_0, y_0)$	
5	Concentration gradient	$\left(\dfrac{\partial c}{\partial y}\right)_{x=x_0, y=y_0}$	The concentration gradient at the interface along y direction
6	Interface position	y_0	The coordinate of the Li/electrolyte interface
7	Lithium growth rate	$\dfrac{y(x_0, t_i) - y(x_0, t_{i-1})}{t_i - t_{i-1}}$	Lithium growth rate at t_i

lithium metal part were replaced by that in the electrolyte adjacent to the lithium surface, followed by 2D Kernel smoothing with a kernel size of [6, 6] to remove background noise.

The seven parameters explored in this study were determined based on the 2D [Li$^+$] mapping in the electrolyte after smoothing. Analytical expressions of these parameters are shown in Table I, and the procedure of numerical calculation of these parameters is presented in the supporting information. For a given point on the lithium surface at a chosen time t_i ($y_0 = y(x_0, t_i)$), the seven input features can be grouped into three categories: 1) Curvatures. The up curvature, curvature, and down curvature of lithium surface, defined as $\dfrac{\partial y}{\partial x}$ at $x = x_0 - 1$, x_0 and $x_0 + 1$, respectively. 2) Concentration-related information, such as [Li$^+$] on lithium surface ($c(x_0, y_0)$), and the gradient of [Li$^+$] along the y direction, $\dfrac{\partial c}{\partial y}$. 3) lithium growth-related information, such as interface position (y_0) and v at t_i and t_{i-1}. The goal is to use these input features to predict v at the next moment t_{i+1}.

These seven features are chosen because they could affect lithium growth physically. Small surface curvature causes tip effect and enhances local electrical field, which can promote local lithium growth. Low ion concentration has two opposite effects on lithium growth. First, it increases the local electrical field based on the diluted electrolyte theory, which promotes lithium growth.[39] Second, it decreases the equilibrium potential for lithium deposition based on the Nernst equation, so that overpotential for lithium deposition decreases. v at prior moments t_i and t_{i-1} may not have a direct causal relationship with v at the next moment t_{i+1}. However, a higher v at t_i and t_{i-1} indicate that lithium prefers to be deposited at this location due to implicit reasons (e.g. curvature, concentration, SEI composition), so that it is possible to enhance v at t_{i+1}.

Artificial neural network (ANN) Model.—We use an ANN model with either one or two hidden layers to learn the relations between input variables at t_i and t_{i-1} and lithium growth rate v at t_{i+1}. The ANN models with one and two hidden layers express the following mathematical relations in Eqs. 1 and 2 below, respectively:

$$v = v(X) = F_1(A_1X + B_1) + B_2 \qquad [1]$$

and

$$v = v(X) = F_2(A_2 \times F_1(A_1X + B_1) + B_2) + B_3, \qquad [2]$$

where F_1 and F_2 are activation functions (in practice, we use the tanh function $F_1(x) = F_2(x) = \frac{e^x - e^{-x}}{e^x + e^{-x}}$), X is the input feature vector as in

Table I, and v is the output. A_1 and A_2, B_1, B_2 and B_3 are the weight matrices and bias vectors, respectively. To keep the distribution of inputs in a comparable range, all features were normalized to the range of $[-1, 1]$. The ANN model was trained by the standard backpropagation method to obtain the weight and bias matrices. Among the 4,000 data points, we use the standard cross-validation approach: 75% were randomly selected for training, and the 25% left were used for testing. The training process uses Bayesian regularization backpropagation algorithm which terminates under multiple stopping conditions,[40] including the maximum epoch number 1000, minimum performance gradient $< 10^{-7}$, and maximum adaptive value $> 10^{10}$.

Sensitivity analysis.—In order to understand the sensitivity of a specific feature, we performed a sensitivity analysis based on the optimized ANN. The sensitivity of v to a specific feature (X_m) is defined as $\left|\dfrac{\partial v}{\partial X_m}\right|$, and numerically it is calculated as

$$s_m(i) = \left| \frac{v(X_m(i) + 0.001) - v(X_m(i) - 0.001)}{0.002} \right| \qquad [3]$$

where the subscript m represents the m th feature, and i means the i th data point. Therefore, there are 4,000 data points for each feature. Their average values and standard deviations were calculated accordingly, which are denoted as $\overline{s_m}$ and Δs_m, respectively. Since X_m is normalized to $[-1, 1]$, the unit of all $s_m(i)$ is μm min^{-1}, which will be neglected in the discussion.

Results and Discussion

Processing of SRS images.—Figure 2a shows a raw SRS image of ion depletion near a lithium metal electrode, where the shining part represents the Li/electrolyte interface due to strong light scattering at the edge of lithium metal. Based on the procedure outlined above, this interface was identified and the [Li$^+$] distribution in the electrolyte was smoothened, as shown in Fig. 2b. This extracted interface is consistent with that in the raw SRS image, validating the accuracy of our image processing. With the same procedure, all lithium metal/electrolyte interfaces were determined in all three data sets. The results in data set 1 are overlapped together and shown in Fig. 2c. The result in Fig. 2b corresponds to $t = 8$ in Fig. 2c, which is highlighted in bold. Moreover, the evolution of lithium boundaries at different moments can be further divided into three stages as indicated by blue, green, and red, which show distinct average v ($\sim$0.04 μm min^{-1} for blue, 0.41 μm min^{-1} or green, and 0.64 μm min^{-1} for red, respectively). These three stages align well with the status of [Li$^+$] on the lithium surface, which are no ion depletion, partial ion depletion, and full ion depletion, respectively.
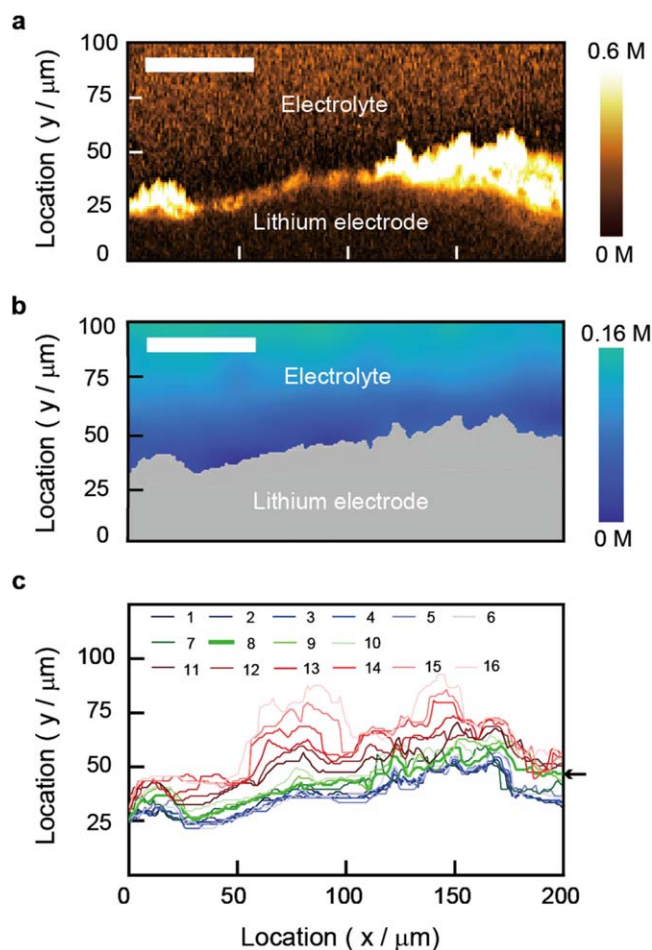
Figure 2. (a) A raw 2D SRS image of ion depletion in the electrolyte near a lithium metal electrode in a Li/gel electrolyte/Li symmetric cell. The dark part at the bottom represents the lithium metal and the shining area is the interface between lithium metal and the electrolyte, while the upper part is the electrolyte. The corresponding color bar represents [Li$^+$]. (b) The lithium electrode and [Li$^+$] in the electrolyte after kernel smoothing. (c) The 16 consecutive lithium boundaries in data set 1. Blue, green and red color correspond to the three stages of lithium metal growth: no [Li$^+$] depletion, partial [Li$^+$] depletion, and full [Li$^+$] depletion, respectively. The scale bars in (a) and (b) are both 50 μm.

Such observations are consistent with our previous imaging results.[27]

Machine Learning Models.—After the Li/electrolyte interface was determined and the [Li$^+$] profile in the electrolyte was smoothened, the seven features in Table I were calculated at each point and each moment. Then they were fed into an ANN for training, validation, and testing. To better illustrate the capability of ANN in this analysis, we will first present fitting results of two cases with different input parameters and network structures, one with poor results and one with good results. Then a detailed analysis on how input parameters, selections of timesteps, and network structures impact fitting capability will be illustrated.

Results of two ANNs with different inputs and network structures are presented in Fig. 3, which show entirely different fitting accuracies. The first one is based on features 4 and 5 at t_i only and a single-layer network with eight neurons (Fig. 3a/b), and the second one is based on all features 1–7 at both t_i and t_{i-1}, and a two-layer network with sixteen neurons in each layer (Fig. 3c/d). In each network, the predicted value (y axis) vs experimental value (x axis) for the training/validation data set and the testing data set are presented in sequence. The correlation coefficient (R) of the testing

datasets of the two networks clearly shows that more features, more time steps, and more complicated ANN structures result in better fitting accuracy of v (0.80 vs 0.32). Moreover, an R-value of 0.93 for training/validation and 0.80 for testing in network 2 are good values for ANN modeling, indicating that the model has a reasonably high fitting accuracy. In addition, the better fitting power of network 2 is also illustrated in the comparison of experimental and predicted values at randomly selected data points across all three datasets, as shown in Fig. 3e/f, where blue and red curves are experimental data and fitting results, respectively. It is clear that network 2 leads to much better fitting results compared to network 1.

To better understand how different factors influence the fitting power of ANN and to validate that network 2 above is efficient, we trained models with various selections of features, numbers of timesteps, and neural network structures, and calculated R of testing data in each case. For the selection of features, four kinds of combinations were considered: 1) features 1–3, which are all related to curvature, 2) features 4 and 5, which are both related to [Li$^+$], 3) features 6 and 7, which are both related to lithium growth, and 4) all the features together. For the number of timesteps, features at t_{i-1} only, t_i only, and both t_{i-1} and t_i were explored as three conditions to predict $v(t_{i+1}) = [y(t_{i+1}) - y(t_i)]/(t_{i+1} - t_i)$. For the neural network structure, a single-layer with eight or sixteen neurons, and two layers with eight or sixteen neurons in each layer were considered, and they are denoted as 8, 16, [8, 8], [16, 16] respectively. Hence, there are total $4 \times 3 \times 4 = 48$ combinations explored.

R of the testing data in these 48 combinations are plotted in Fig. 4. Figures 4a–4c correspond to using data at t_{i-1} only, t_i only, and both t_{i-1} and t_i, respectively. The results show that only using curvature features (1–3) renders a low R of less than 0.2, even if information at both t_{i-1} and t_i was used. [Li$^+$]-based features (4 and 5) are more important, which gives higher R up to 0.38–0.45, when the information at both t_{i-1} and t_i was used. Features related to solid lithium growth at prior time steps (6 and 7) also result in a higher R of 0.33–0.71. Especially when features 6 and 7 at both t_{i-1} and t_i were used, R reached 0.71 with a [16, 16] ANN. These results indicate that [Li$^+$] and v at prior moments are more critical to v at the next moment than the mesoscale surface curvatures obtained from SRS images. However, it should be noted that such curvature may not precisely reflect the nanoscale curvature at the lithium tip. Besides the varying importance of different features, the structure of ANN also affects the model accuracy remarkably. [16, 16] ANN performs much better than single-layer networks and the [8, 8] ANN. However, when the complexity of ANN is further increased, the accuracy of the prediction even decreases and the overfitting problem becomes overwhelming (Fig. S5). Hence, we don't further explore more complicated neural network structures. More details can be found in the supporting information.

Figure 4 also shows that the accuracy of ANN can be further enhanced by taking all features into account, which echoes the results in Fig. 3. When only information at t_i is taken into account, R reaches 0.71 with a bilayer ANN of [16, 16]. R further increases to 0.80 when the information at both t_{i-1} and t_i is considered, which is reasonably high for fitting v by information extracted from SRS images. Therefore, in the following discussion, the optimized ANN model with all features from t_{i-1} and t_i, and a bilayer neural network of [16, 16] is used, which is network 2 in Fig. 3c/d.

Sensitivity analysis.—The different R values in Fig. 4 suggest that the impact of these features on v is different. To quantitatively evaluate their impacts, we calculated the sensitivity of v to each feature, which is defined as $s_m = |\frac{\partial v}{\partial x_m}|$ based on network 2 above. Since s_m varies from one data point to another, we plot the distribution of s_m in a single run of ANN fitting (Fig. 5). Figures 5a and 5b are the distribution of s_1 to s_7 at t_{i-1} and t_i, respectively, and Fig. 5c shows the corresponding $\overline{s_m}$ and Δs_m for these 14 features. From the results, we can clearly see that v is insensitive to the curvature of the lithium surface (features 1–3), but
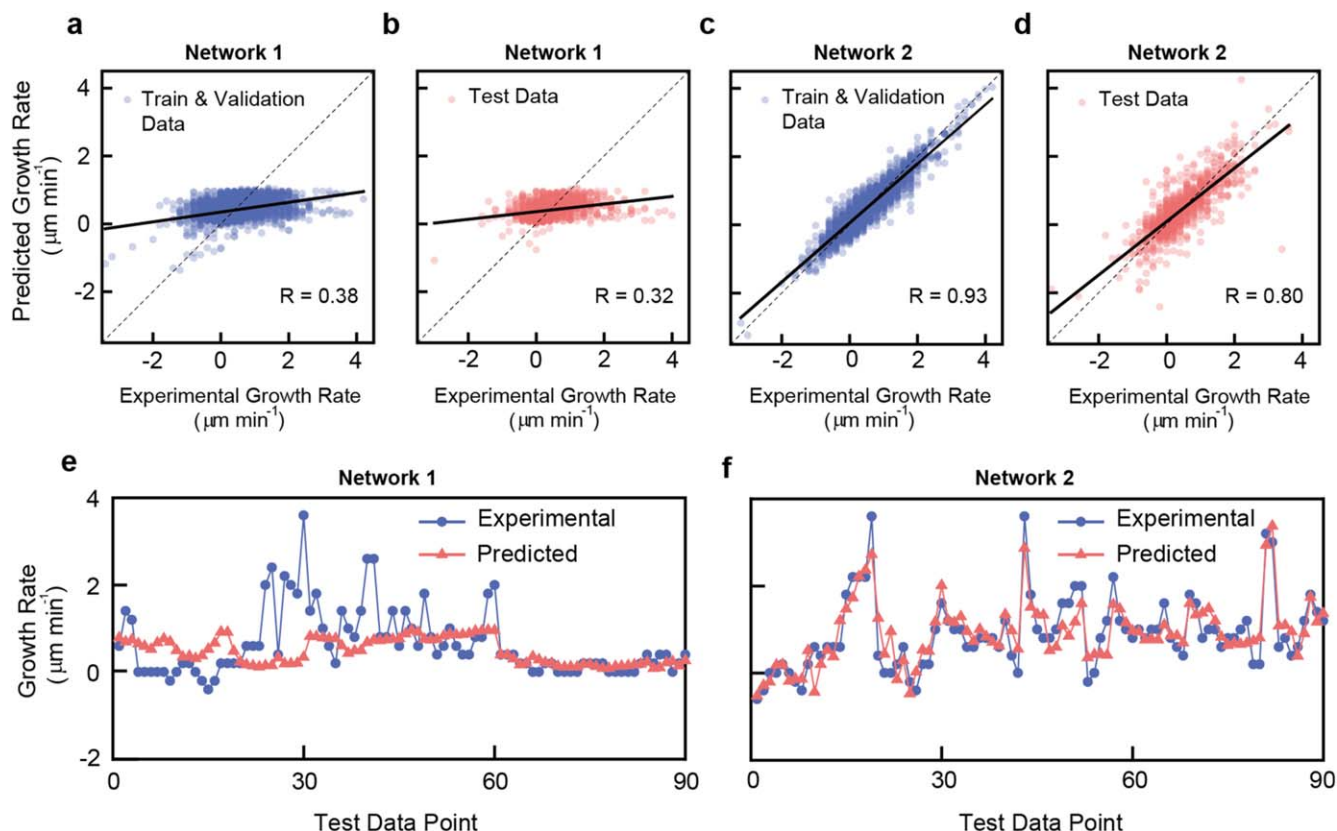
Figure 3. Fitting results of two different ANNs with different input features and network structures. Network 1 is a single-layer network with eight neurons, and features 4 and 5 at t_i are used as the input. Network 2 is a two-layer network with sixteen neurons in each layer, and features 1–7 at both t_i and t_{i-1} are used as the input. (a/b) The fitting results of (a) training/validation data set and (b) testing data set of network 1. (c/d) The fitting results of (c) training/validation data set and (d) testing data set of network 2. All data points across all three datasets are drawn in the figure. (e/f) The fitting results and experimental true values for randomly selected points in the testing data sets with (e) network 1 and (f) network 2.
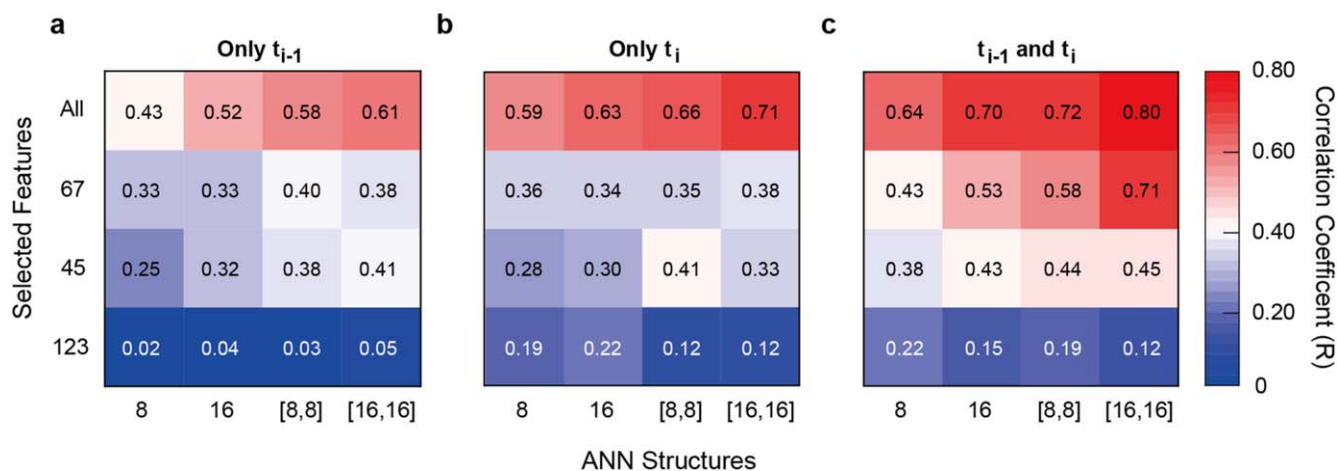
Figure 4. The correlation coefficient (R) of predicted values vs experimental values in the testing data set only. They correspond to 48 combinations with different ANN structures, selected features, and time-steps for (a) only t_{i-1}, (b) only t_i and (c) both t_{i-1} and t_i. The R-value in each square is the averaged R of five different runs of data fitting, which helps minimize fluctuations in data fitting. The definition of features is the same as table 1. 8, 16, [8, 8] and [16, 16] in the *x*-axis label are different network structures defined in the section of Methods.

it is more sensitive to concentration and growth rate-related features (4–7). The weak correlation between the Li/electrolyte interface curvatures and *v* may partially arise from the precision loss during image capturing and processing. With further improvement of the spatial resolution of SRS microscopy and better interface recognition algorithms, the correlation between the Li/electrolyte interface curvature and *v* could be better unveiled.

We also found that different runs of ANN fitting generated different fitting parameters, which is common in neural networks. Although these runs result in similar R values in both training/validation data and testing data, s_m in different runs could vary to some extent (Fig. S2). Therefore, we performed the model training process 100 times and calculated $\overline{s_m}$ in each training. The average and the standard deviation of $\overline{s_m}$ in such 100 runs of training are
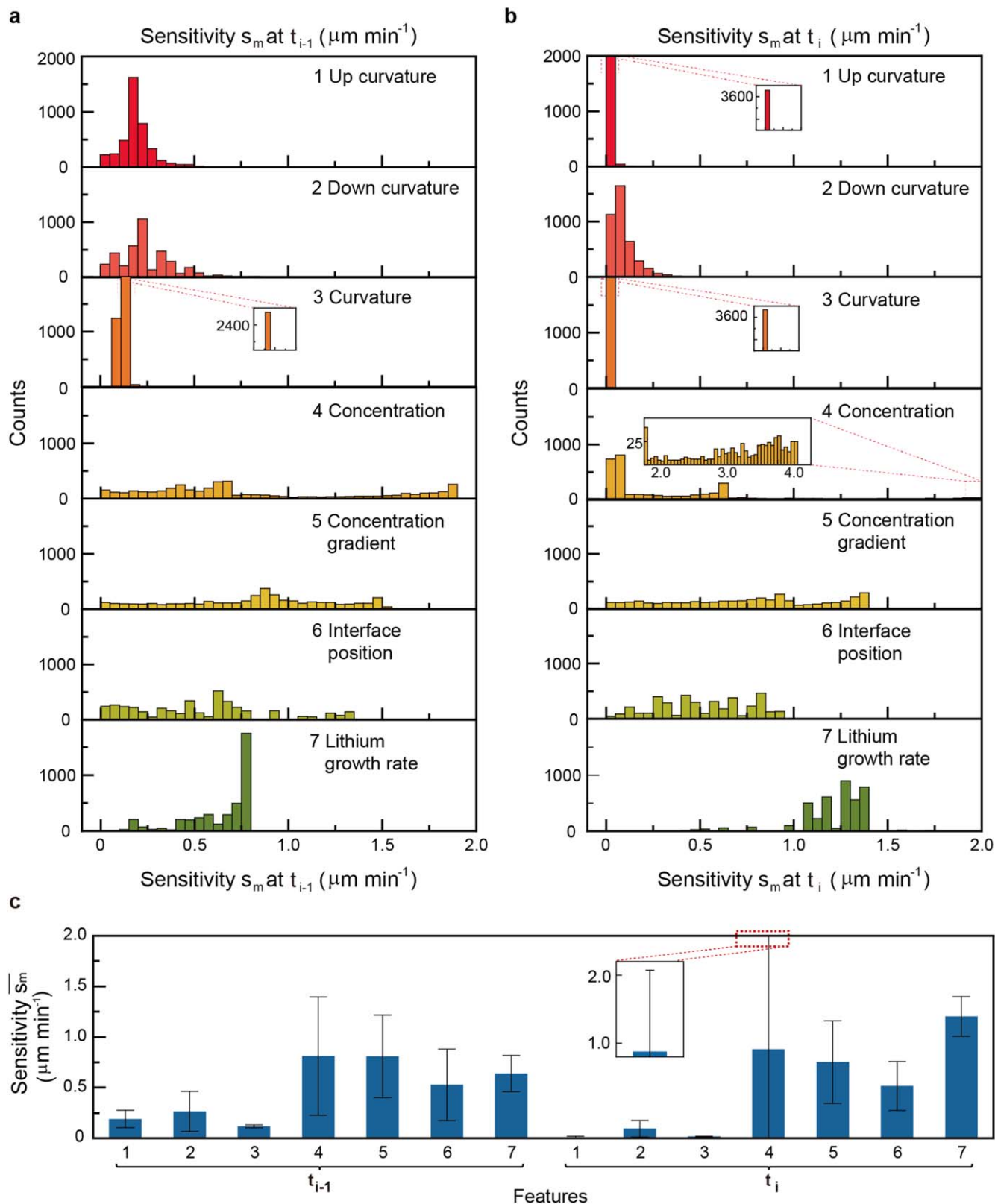
Figure 5. (a/b) The distribution of sensitivity s_m to fitting features 1–7 at (a) t_{i-1} and (b) t_i in the optimized [16,16] ANN. (c) Corresponding $\overline{s_m}$ and Δs_m for features 1–7 at t_{i-1} and t_i. The seven features are the same as those in table 1: (1) up curvature, (2) down curvature, (3) curvature, (4) [Li$^+$] at the interface, (5) concentration gradient, (6) interface position, and (7) lithium growth rate.

denoted as $\overline{s_m}$ and $\Delta \overline{s_m}$, respectively, and they are plotted as Fig. 6a. The results are similar to those in a single run in Fig. 5c. Again, [Li$^+$]-related features (4/5) and lithium growth-related features (6/7) at prior moments (t_{i-1} and t_i) influence v at t_{i+1} most.

Such results may be explained as follows. First, 1D transport theory of a diluted electrolyte shows that $E = -\frac{D_{eff}}{F}\frac{1}{c}\frac{dc}{dy}$, where E is the local electrical field, D_{eff} is the effective diffusivity of ions in the
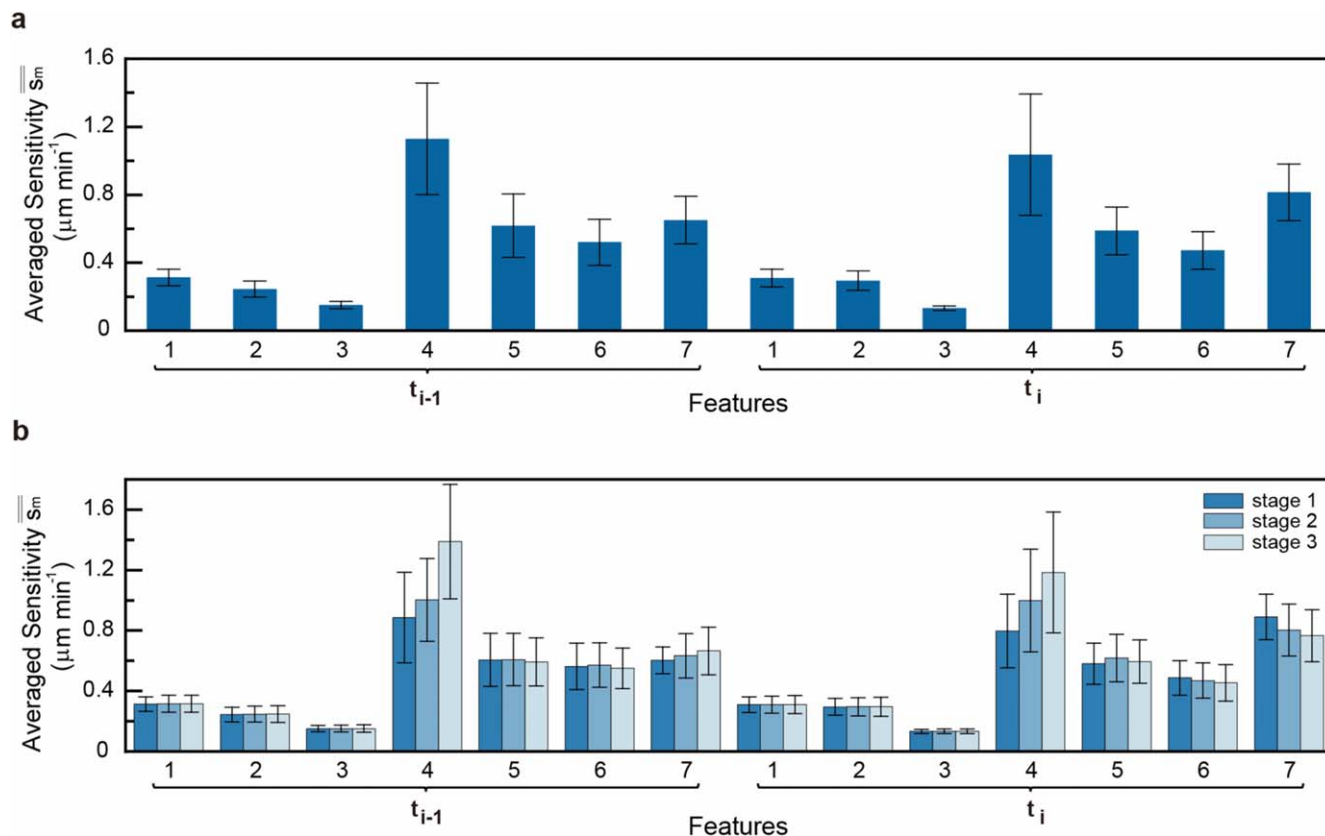
Figure 6. The averaged sensitivity of the seven features at t_{i-1} and t_i with each feature's standard deviation as the error bar. (a) $\overline{s_m}$ and $\Delta\overline{s_m}$ of 100 runs of training based on all three datasets. (b) $\overline{s_m}$ and $\Delta\overline{s_m}$ in three stages based on 100 runs of training. The three stages are no ion depletion, partial ion depletion, and full ion depletion, respectively.

electrolyte, and F is the Faraday constant.[39] Therefore, a lower c results in a larger E, which promotes lithium growth and thus a larger v. Conversely, a larger v at previous moments suggests a lower c at the local interface or lower local SEI impedance, which facilitates fast lithium growth at the next moment. In addition, it is generally agreed that lower salt concentration leads to poorer SEI since a high portion of electrolyte decomposition products does not result in good mechanical properties of SEI.[41] This could be another reason why v is sensitive to c.

Regarding the relatively high sensitivity to lithium growth at prior moments (features 6 and 7), it is likely that a higher v at prior moments t_i and t_{i-1} indicate that lithium prefers to be deposited at this location due to implicit reasons (e.g. curvature, concentration, SEI composition), which lead to a high v at t_{i+1} too.

The analysis so far is based on analyzing the entire process as a whole. However, as discussed in literature[11,27] and Fig. 2, lithium growth undergoes different stages, such as mossy lithium when ions are not depleted, transitional growth when ions are partially depleted, and dendritic growth when ions are fully depleted. Therefore, it is possible that s_m varies across the three stages. To understand if s_m is stage-sensitive, we analyzed s_m in each stage separately, as shown in Fig. 6b. In all three stages, v is most sensitive to features 4 and 7, moderately sensitive to features 5 and 6, but insensitive to features 1–3. Such results indicate that concentration and growth rate at the prior moments are important at all stages, which agrees with analyses above based on all three stages together. The insensitivity to curvature-related features 1–3 needs further investigation, since the mesoscale curvature may not accurately reflect the real curvature at a finer scale. Moreover, we also observe that the sensitivity to feature 4 (concentration) is slightly higher in stages 2 and 3. For example, s_4 at t_i increases from 0.80 ± 0.24 in stage 1 to 1.00 ± 0.34 in stage 2 and 1.18 ± 0.40 in stage 3. This is

consistent with our previous observations that the correlation coefficient between concentration and v becomes higher upon ion depletion.

The higher sensitivity at a later stage could be explained based on the relation between v, E and c. As E is proportional to $\frac{1}{c}\frac{dc}{dy}$, and thus $\delta E/\delta c$, the variation of E due to variation of c, is proportional to $-\frac{1}{c^2}\frac{dc}{dy} + \frac{1}{c}\delta\left(\frac{dc}{dy}\right)/\delta c$. The first term becomes larger at a lower c. The second term also gets larger at a lower c, since dc/dy is higher at stronger depletion. As the two terms have the same signs, $\delta E/\delta c$ becomes larger at a lower c. Moreover, since E is positively correlated with v, the sensitivity of v to c ($\delta v/\delta c$) should be positively correlated with $\delta E/\delta c$, which is higher at a lower c and thus a later stage.

Besides gaining fundamental understanding by using an optical cell, it is also important to discuss how such strategies can be transferred to practical cells. We think that there are several possible directions to explore. First, by reducing lithium-lithium distance to ~10–50 μm, wrapping lithium with a piece of separator (Fig. S6), and even applying pressure onto the cell envelope, the optical cell can better mimic processes in real cells. Second, developing strategies to probe concentration variation in real cells. Ultrathin optical fiber-based detection of ion concentration in a practical cell was reported recently.[42] Synchrotron may also detect concentration polarization in real cells in principle. If these techniques can be further advanced to multiple points and faster speed, respectively, they have the potential to monitor concentration polarization in a real cell. Meanwhile, Synchrotron can image lithium metal growth in real cells,[43] so that heterogeneity in salt concentration could be correlated with lithium growth. The third direction is to consider how to use machine learning methods to predict lithium growth from other

parameters. For example, it is possible to image the 2D distribution of pressure by a pressure sensor array and temperature in a cell by X-ray diffraction.[44] Then if lithium growth can be imaged by either in situ Synchrotron imaging or optical imaging through opening a real cell, it is possible to use ANN to set up connections between these new parameters and lithium growth. It would be exciting to realize machine learning models to predict lithium growth in practical cells.

Conclusions

Thanks to the capability of mapping electrolyte concentration provided by SRS microscopy, we carried out neural network-based modeling to understand the relation between lithium growth and local material properties, such as salt concentration and surface curvatures, which has been done for the first time to the best of our knowledge. ANN successfully fits the lithium growth rate based on various features related to curvature, local salt concentration, and lithium growth rate at prior moments. In an optimized ANN, the correlation coefficient between predicted values and experimental values reaches 0.80 for the testing data set. Further sensitivity analysis of the ANN model indicates that $[Li^+]$ and its gradient near the Li/electrolyte interface as well as the growth rate at prior moments act as dominant factors in determining lithium dendrite growth rate at the next moment. Our study shows that neural network models have a potential capability to forecast lithium growth rate and provide insight into how the growth rate is sensitive to various factors, which is often hidden by the sophisticated reaction mechanism and lacks model confirmation for a long time. We believe that with further optimization, machine learning-based methods can provide deeper insights into lithium metal growth and address this important issue.

List of symbols

v	Lithium growth rate
R	Pearson correlation coefficient
t_{i-1}, t_i, t_{i+1}	Previous, present and next moment
X	Input feature vector in ANN model
A, B	Weight and bias matrix in ANN model
F	Activation function in ANN model
m	Feature number
s_m	Sensitivity, $\mu m\ min^{-1}$
$\overline{s_m}$	Average sensitivity, $\mu m\ min^{-1}$
$\overline{\overline{s_m}}$	Average sensitivity in 100 runs of training, $\mu m\ min^{-1}$
Δs_m	Standard deviation of sensitivity, $\mu m\ min^{-1}$
$\overline{\Delta s_m}$	Standard deviation of sensitivity in 100 runs of training, $\mu m\ min^{-1}$

ORCID

Yirui Ma ⓘ https://orcid.org/0000-0001-5410-6642
Yuan Yang ⓘ https://orcid.org/0000-0002-4355-5474

References

1. D. Lin, Y. Liu, and Y. Cui, *Nat. Nanotechnol.*, **12**, 194 (2017).
2. P. Albertus, S. Babinec, S. Litzelman, and A. Newman, *Nat. Energy*, **3**, 16 (2017).
3. J. Liu et al., *Nat. Energy*, **4**, 180 (2019).
4. H. Liu, X.-B. Cheng, Z. Jin, R. Zhang, G. Wang, L.-Q. Chen, Q.-B. Liu, J.-Q. Huang, and Q. Zhang, *EnergyChem*, **1**, 100003 (2019).
5. H. Kim, G. Jeong, Y.-U. Kim, J.-H. Kim, C.-M. Park, and H.-J. Sohn, *Chem. Soc. Rev.*, **42**, 9011 (2013).
6. W. Li, H. Yao, K. Yan, G. Zheng, Z. Liang, Y.-M. Chiang, and Y. Cui, *Nat. Commun.*, **6**, 7436 (2015).
7. M. D. Tikekar, S. Choudhury, Z. Tu, and L. A. Archer, *Nat. Energy*, **1**, 16114 (2016).
8. J. Xiao, *Science*, **366**, 426 (2019).
9. Z. Liu, Y. Qi, Y. X. Lin, L. Chen, P. Lu, and L. Q. Chen, *J. Electrochem. Soc.*, **163**, A592 (2016).
10. B. Wu, J. Lochala, T. Taverne, and J. Xiao, *Nano Energy*, **40**, 34 (2017).
11. P. Bai, J. Li, F. R. Brushett, and M. Z. Bazant, *Energy Environ. Sci.*, **9**, 3221 (2016).
12. S. Yuan, J. L. Bao, J. Wei, Y. Xia, D. G. Truhlar, and Y. Wang, *Energy Environ. Sci.*, **12**, 2741 (2019).
13. J. Tan, A. Cannon, and E. Ryan, *J. Power Sources*, **463**, 228187 (2020).
14. Y. Lee, B. Ma, and P. Bai, *Energy Environ. Sci.*, **13**, 3504 (2020).
15. X. Wang, W. Zeng, L. Hong, W. Xu, H. Yang, F. Wang, H. Duan, M. Tang, and H. Jiang, *Nat. Energy*, **3**, 227 (2018).
16. F. Han, A. S. Westover, J. Yue, X. Fan, F. Wang, M. Chi, D. N. Leonard, N. J. Dudney, H. Wang, and C. Wang, *Nat. Energy*, **4**, 187 (2019).
17. H.-K. Tian, Z. Liu, Y. Ji, L.-Q. Chen, and Y. Qi, *Chem. Mater.*, **31**, 7351 (2019).
18. X.-B. Cheng, C.-Z. Zhao, Y.-X. Yao, H. Liu, and Q. Zhang, *Chem*, **5**, 74 (2019).
19. A. Jana, S. I. Woo, K. S. N. Vikrant, and R. E. García, *Energy Environ. Sci.*, **12**, 3595 (2019).
20. Y. Li et al., *Science*, **358**, 506 (2017).
21. D. S. Eastwood et al., *Chem Commun (Camb)*, **51**, 266 (2015).
22. H. J. Chang, A. J. Ilott, N. M. Trease, M. Mohammadi, A. Jerschow, and C. P. Grey, *JACS*, **137**, 15209 (2015).
23. Q. Cheng, Y. Miao, J. Wild, W. Min, and Y. Yang, *Matter*, **4**, 1460 (2021).
24. Q. Cheng et al., *ChemRxiv* (2021), https://chemrxiv.org/engage/chemrxiv-article-details/60c754c29abda27b7af8e229.
25. L. Wei, F. Hu, Y. Shen, Z. Chen, Y. Yu, C. C. Lin, M. C. Wang, and W. Min, *Nat. Methods*, **11**, 410 (2014).
26. W. Min, C. W. Freudiger, S. Lu, and X. S. Xie, *Annu. Rev. Phys. Chem.*, **62**, 507 (2011).
27. Q. Cheng et al., *Nat. Commun.*, **9**, 2942 (2018).
28. V. S. Dave and K. Dutta, *Artif. Intell. Rev.*, **42**, 295 (2014).
29. I. Yılmaz and A. J. R. M. Yuksek, *R. Mechanics and R. Engineering*, **41**, 781 (2008).
30. M. S. Nasr, M. A. E. Moustafa, H. A. E. Seif, and G. El Kobrosy, *Alexandria Engineering Journal*, **51**, 37 (2012).
31. A. Ali, A. Abdulrahman, S. Garg, K. Maqsood, and G. Murshid, *Greenhouse Gases: Science and Technology*, **9**, 67 (2019).
32. O. I. Abiodun, A. Jantan, A. E. Omolara, K. V. Dada, N. A. Mohamed, and H. Arshad, *Heliyon*, **4**, e00938 (2018).
33. Y. Zhang, R. Xiong, H. He, and M. G. Pecht, *IEEE Trans. Veh. Technol.*, **67**, 5695 (2018).
34. L. Ren, L. Zhao, S. Hong, S. Zhao, H. Wang, and L. Zhang, *IEEE Access*, **6**, 50587 (2018).
35. C. Chen, R. Xiong, R. Yang, W. Shen, and F. Sun, *J. Clean. Prod.*, **234**, 1153 (2019).
36. M. Ismail, R. Dlyma, A. Elrakaybi, R. Ahmed, and S. Habibi, *IEEE Transportation Electrification Conference and Expo (ITEC)*, p. 342 (2017).
37. I. Rey, J. L. Bruneel, J. Grondin, L. Servant, and J. C. Lassègues, *J. Electrochem. Soc.*, **145**, 3034 (1998).
38. C. Brissot, M. Rosso, J. N. Chazalviel, and S. Lascaud, *J. Electrochem. Soc.*, **146**, 4393 (1999).
39. J. Newman and K. E. Thomas-Alyea, *Electrochemical Systems, Wiley* (Wiley , New Jersey, NJ) (2012).
40. F. Burden and D. Winkler, *Artificial Neural Networks: Methods and Applications*, ed. D. J. Livingstone (Humana Press, Totowa, NJ) p. 23 (2009).
41. X. Ren et al., *Proc Natl Acad Sci U S A*, **117**, 28603 (2020).
42. T. Yamanaka, H. Nakagawa, S. Tsubouchi, Y. Domi, T. Doi, T. Abe, and Z. Ogumi, *ChemSusChem*, **10**, 855 (2017).
43. S.-H. Yu, X. Huang, J. D. Brock, and H. D. Abruña, *JACS*, **141**, 8441 (2019).
44. X. Yu, Z. Feng, Y. Ren, D. Henn, Z. Wu, K. An, B. Wu, C. Fau, C. Li, and S. J. Harris, *J. Electrochem. Soc.*, **165**, A1578 (2018).